

Theoretical analysis of measurement crosstalk for coupled Josephson phase qubits

Abraham G. Kofman,^{1,*} Qin Zhang,¹ John M. Martinis,² and Alexander N. Korotkov¹
¹*Department of Electrical Engineering, University of California, Riverside, California 92521, USA*
²*Department of Physics, University of California, Santa Barbara, California 93106, USA*

(Received 23 June 2006; revised manuscript received 28 November 2006; published 23 January 2007)

We analyze the crosstalk error mechanism in measurement of two capacitively coupled superconducting flux-biased phase qubits. The damped oscillations of the superconducting phase after the measurement of the first qubit may significantly excite the second qubit, leading to its measurement error. The first qubit, which is highly excited after the measurement, is described classically. The second qubit is treated both classically and quantum mechanically. The results of the analysis are used to find the upper limit for the coupling capacitance (thus limiting the frequency of two-qubit operations) for a given tolerable value of the measurement error probability.

DOI: [10.1103/PhysRevB.75.014524](https://doi.org/10.1103/PhysRevB.75.014524)

PACS number(s): 74.50.+r, 03.67.Lx, 85.25.Cp

I. INTRODUCTION

Superconducting Josephson-junction circuits, including phase,¹ flux,² and charge³ qubits, have attracted a significant interest as promising devices for quantum information processing.⁴ In this paper we consider flux-biased phase qubits,⁵⁻⁷ which have been introduced relatively recently and have a clear advantage over the current-biased phase qubits. While the schematic of a flux-biased phase qubit (Fig. 1) may be very similar to a flux qubit (in the simplest case, a superconducting loop interrupted by one Josephson junction), an important difference is that in the phase qubit the logic states $|0\rangle$ and $|1\rangle$ are represented by two lowest levels in one well of the corresponding potential profile, while for the flux qubit the levels in two neighboring wells are used. An imaginary-swap quantum gate, which together with single-qubit rotations forms a universal set of quantum gates,⁸ has been realized with flux-biased phase qubits in Ref. 9. The Bell-type correlations in measurement of two phase qubits¹⁰ and the quantum state tomography¹¹ for phase qubits have also been demonstrated recently.

The measurement of qubits is an important stage in quantum information processing, representing one of numerous challenges on the way to a scalable quantum computer. The measurement techniques are constantly improving and new ways of qubit measurement are being introduced; for example, an idea of “dispersive” readout schemes has been recently proposed and realized for superconducting charge

qubits.¹² For flux-biased phase qubits a scheme allowing fast measurement has been recently implemented.^{6,9-11} According to this scheme, a measurement pulse lowers the barrier between the shallow (“left”) potential well used for qubit states and a much deeper “right” well (Fig. 1), so that during the pulse a qubit in the upper state $|1\rangle$ switches by tunneling to the right-hand well with probability close to one, while a qubit in the lower state $|0\rangle$ remains intact. A little later a nearby SQUID is switched on to detect in which well the qubit is localized, that completes the measurement.

Simultaneous measurement of two capacitively coupled phase qubits is complicated by crosstalk,⁹ which is caused by the fact that in the simple design realized experimentally so far (Fig. 2) the qubit coupling is fixed and therefore qubits remain coupled in the process of measurement. The crosstalk mechanism is the following. Suppose that one of the qubits is measured in state $|1\rangle$, which means tunneling to the right well. The tunneling is then followed by the dissipative evolution (damped oscillations), eventually reaching the ground state of the right well. These oscillations perturb the state of the second, capacitively coupled qubit, especially because in the experiment the oscillation frequencies in both wells are somewhat close to each other, and both qubits are practically identical. Therefore, if the measurement pulse is applied to the second qubit after the dissipative evolution of the first qubit, the measurement result is likely to be wrong: the second qubit in state $|0\rangle$ will often be read out as in state $|1\rangle$ because of the second qubit excitation.⁹ To avoid this problem, the measurement pulses should be applied to both qubits almost simultaneously,⁹ within the time scale shorter than development of the crosstalk mechanism.

However, this is not a complete solution of the problem because the excitation of the second qubit due to crosstalk

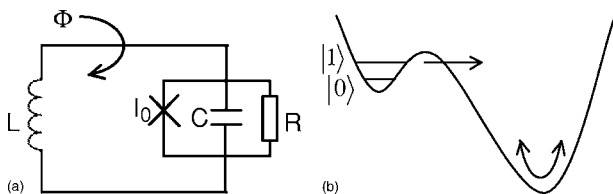


FIG. 1. The circuit schematic of a flux-biased phase qubit and the corresponding potential profile (as a function of the phase difference δ across the Josephson junction). During the measurement the state $|1\rangle$ escapes from the “left” well through the barrier, which is followed by oscillations in the “right” well. This dissipative evolution leads to the two-qubit crosstalk.

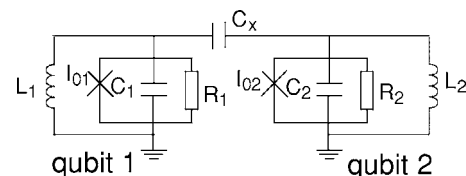


FIG. 2. The circuit schematic for two capacitively coupled flux-biased phase qubits.

may be sufficient to switch the qubit from the left well to the right well even a little *after* the second-qubit measurement pulse; such switching will also lead to the measurement error because the readout SQUID distinguishes the left/right states significantly later (microsecond scale). This type of error will be of the main interest in our paper.

We emphasize that the crosstalk mechanism considered here is due to a fixed coupling between the qubits. It seems possible to realize schemes with adjustable coupling in the future, which will eliminate much of the measurement crosstalk discussed here. Still, it is of interest to analyze the fixed-coupling case, since this is the simplest scheme and the only one realized experimentally so far.

In this paper we analyze the measurement crosstalk mechanism for two capacitively coupled flux-biased phase qubits (Fig. 2), and calculate the corresponding measurement error. In Sec. II we discuss the system to be studied. The measurement crosstalk is analyzed in Secs. III–V. For definiteness, we assume that the first qubit is switched (from state $|1\rangle$), while the second qubit is initially in the state $|0\rangle$. The dynamics of the first qubit, which after the switching performs damped oscillations in the deep well, is analyzed classically in Sec. III. Such an approximation drastically simplifies the problem and is also quite accurate, since for the experimental parameters⁹ used here the first qubit is highly excited after measurement, with typical quantum number over 10^2 . The second qubit in this paper is treated both classically and quantum mechanically. The classical treatment (Sec. IV) includes two approaches: the harmonic-oscillator model,⁹ which allows for an analytical treatment, and a numerical solution for the exact (anharmonic) potential profile of the qubit. The results of the quantum approach are presented in Sec. V; to a significant extent their understanding can be based on the results of the classical analysis. In the quantum approach we completely neglect dissipation in the second qubit; however, insight is given by the classical approach. The conclusions are summarized in Sec. VI. The appendices mostly contain mathematical details. In particular, basic properties of the one-qubit potential are reviewed in Appendix A, the Hamiltonian for two capacitively coupled qubits is derived in Appendix B, the first-qubit dynamics after switching is discussed in Appendix C, the details of the classical approach for the second-qubit dynamics are presented in Appendix D, and details of the quantum approach are discussed in Appendix E.

II. FLUX-BIASED PHASE QUBITS

A flux-biased phase qubit schematic⁵ coincides with that of the basic rf SQUID (Ref. 13) (Fig. 1). Neglecting dissipation, it can be described¹³ as a fictitious mechanical system with the Hamiltonian

$$H = \frac{p^2}{2m} + U(\delta), \quad (1)$$

where δ is the superconducting phase difference across the Josephson junction, $p = m\dot{\delta}$ is the corresponding momentum, $m = (\Phi_0/2\pi)^2 C$ is the effective mass determined by the ca-

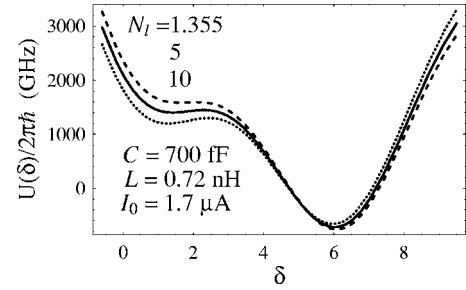


FIG. 3. The qubit potential $U(\delta)$ [Eq. (2)] for $N_l=10$ (dotted line), $N_l=5$ (solid line), and $N_l=1.355$ (dashed line).

pacitance C , $\Phi_0 = h/(2e)$ is the flux quantum, e is the electron charge, and $U(\delta)$ is the potential energy (shown schematically in Fig. 1):

$$U(\delta) = E_J \left[\frac{(\delta - \phi)^2}{2\lambda} - \cos \delta \right]. \quad (2)$$

Here $E_J = \Phi_0 I_0 / 2\pi$ is the Josephson energy, $\lambda = 2\pi I_0 L / \Phi_0$ is the dimensionless inductance, $\phi = 2\pi \Phi / \Phi_0$ is the dimensionless external magnetic flux, I_0 is the critical current, and L is the inductance. In Appendix A we review the basic properties of the potential energy (2).

For numerical calculations presented in this paper we will use the following values of the parameters from the experiment of Ref. 9:

$$C = 700 \text{ fF}, \quad L = 0.72 \text{ nH}, \quad I_0 = 1.7 \text{ } \mu\text{A}. \quad (3)$$

For these parameters $\lambda = 3.72$, and the potential (2) has either one or two wells (see Appendix A) depending on the value of external flux ϕ ; the two-well case is realized at $2\pi - \phi_c < \phi < \phi_c$ [the second well disappears at the critical flux $\phi_c = \pi/2 + \arcsin(1/\lambda)$; see Appendix A]. For definiteness we assume $\pi < \phi < \phi_c$, so that the right well is deeper than the left well.

The depth ΔU_l of the left well (i.e., the difference between the potential maximum and minimum) can be characterized by the crude estimate of the number of discrete levels in the well

$$N_l = \frac{\Delta U_l}{\hbar \omega_l}, \quad (4)$$

where ω_l is the “plasma” frequency (the classical oscillation frequency near the well bottom) for the left well (see Appendix A). Notice that N_l is not necessarily integer and there is no simple relation between N_l and exact number of discrete levels in the well because of significant anharmonicity of the potential. Figure 3 shows the qubit potential $U(\delta)$ for $N_l = 10$ (corresponding to $\phi = 4.842$), $N_l = 5$ ($\phi = 5.089$), and $N_l = 1.355$ ($\phi = 5.308$); the last value corresponds to the bias during the measurement pulse (see below). The qubit levels $|0\rangle$ and $|1\rangle$ are, respectively, the ground and the first excited levels in the left well.

Now let us consider two capacitively coupled flux-biased phase qubits⁹ (Fig. 2). The current balance for this circuit yields the equations

$$\ddot{\delta}_i + \frac{\dot{\delta}_i}{C'_i R_i} + \frac{2\pi I_{0i}}{\Phi_0 C'_i} \sin \delta_i + \frac{\delta_i - \phi_i}{C'_i L_i} = \frac{C_x}{C'_i} \ddot{\delta}_j, \quad (5)$$

where qubits are numbered by $i, j=1, 2 (i \neq j)$; $C'_i = C_i + C_x$; the quantities δ_i , I_{0i} , C_i , and L_i are, respectively, the Josephson-junction phase difference, critical current, capacitance, and inductance for the i th qubit, C_x is the coupling capacitance, and $\phi_i = 2\pi\Phi_i/\Phi_0$ is the dimensionless external magnetic flux. Dissipation in Josephson junctions is described using the resistively shunted junction (RSJ) model¹³ by introducing resistances R_1 and R_2 into the circuit (Fig. 2). For each junction the dissipation can be characterized by the energy relaxation time

$$T_1 = R_1 C_1, \quad T'_1 = R_2 C_2. \quad (6)$$

The derivation of the Lagrangian and Hamiltonian for the two-qubit system is presented in Appendix B. For two identical qubits (when the subscript $i=1, 2$ can be dropped in the qubit parameter notation),

$$C_i = C, \quad L_i = L, \quad I_{0i} = I_0, \quad (7)$$

the system Hamiltonian is (Appendix B)

$$H = \frac{p_1^2 + p_2^2 + 2\zeta p_1 p_2}{2(1 + \zeta)m} + U_1(\delta_1) + U_2(\delta_2), \quad (8)$$

where $\zeta = C_x/(C + C_x)$, the potential energies $U_i(\delta_i)$ of the two qubits [Eq. (2)] are controlled by different fluxes ϕ_i , and the generalized momenta p_i are the total (node) charges on the i th junction and the adjacent coupling capacitor multiplied by $\hbar/2e$.^{13,14} Experimental parameters of Ref. 9, $C_x = 6$ fF and $T_1 = 25$ ns, correspond to $\zeta = 8.5 \times 10^{-3}$ and $R = 35.7$ k Ω .

III. CROSSTALK MECHANISM AND FIRST-QUBIT DYNAMICS

In the fast measurement scheme employed in Refs. 6 and 9, a short flux pulse applied to the measured qubit decreases the barrier between the two wells (see Fig. 1), so that the upper qubit level becomes close to the barrier top. In the case when level $|1\rangle$ is populated, there is a fast population transfer (tunneling) from the left well to the right well. Due to dissipation, the energy in the right well gradually decreases, until it reaches the bottom of the right well. In contrast, if the qubit is in state $|0\rangle$ the tunneling essentially does not occur. The qubit state in one of the two potential minima (separated by almost Φ_0) is subsequently distinguished by a nearby SQUID, which completes the measurement process.

In a system of two identical coupled qubits, crosstalk can produce measurement error if the qubits are in different logical states.⁹ For definiteness, we assume that before the measurement the qubit system is in the state $|10\rangle$, i.e., the first qubit is in the excited state and second qubit is in the ground state. Then after the measurement the first qubit performs damped oscillations in the right well, which in the classical language¹³ produces an oscillating (microwave) voltage $(\Phi_0/2\pi)\dot{\delta}_1(t)$. This voltage causes oscillating current through the coupling capacitor C_x , which perturbs the second

qubit. The effect is so strong that measurement of the second qubit after the dissipative evolution of the first qubit is practically useless: there is a little chance for the second qubit to remain in the ground state.⁹ The effect of crosstalk can be significantly suppressed if the two qubits are measured practically simultaneously (experimentally, not more than few nanoseconds apart) because the crosstalk excitation of the second qubit takes finite time.⁹ Nevertheless, crosstalk leads to noticeable measurement errors even in the case of simultaneous qubit measurement. The reason is that strong excitation of the second qubit may lead to its switching from the left to the right well even in the absence of the measurement pulse. (Recall that the states are distinguished by the SQUID a little later, so switching due to strong excitation is practically indistinguishable from switching during the measurement pulse.)

This is exactly the effect which we analyze in this paper. We assume that the first qubit is switched to the right well at $t=0$, while the second qubit at this time is in the ground state and no measurement pulse is applied to the second qubit (physically, this means that the pulse is short and does not change the qubit state). Our main goal will be analysis of the measurement error, which in this case is switching of the second qubit to the right well due to the crosstalk excitation.

A rigorous theoretical study of the measurement crosstalk should involve a numerical solution of quantum evolution of two coupled qubits accounting for dissipation, which would require extensive computer resources. In the present paper we employ several simplified approaches, which have the advantage of being relatively fast numerically, thus facilitating a study of the crosstalk dependence on the parameters. The first qubit is always treated classically, while the second qubit is studied both classically and quantum mechanically. (Classical treatment of the first qubit is justified by its very strong excitation: for our parameters its energy after switching corresponds to the quantum number $n_1 = 191$, and the interesting part of the dissipative dynamics happens when the corresponding level number in the right well is still very large, $n_1 \approx 30$.)

We will mainly consider two experimentally relevant cases of the second qubit biasing, characterized by the dimensionless barrier heights $N_2 = 5$ and 10 ($\phi_2 = 5.09$ and 4.84, respectively). The corresponding left-well plasma frequencies [see Eq. (A8)] are $\omega_{l2}/2\pi = 8.91$ GHz and 10.2 GHz. The crosstalk mechanism is obviously very efficient when the first qubit oscillation is in resonance with ω_{l2} .

For the first qubit we choose the biasing parameter $N_{l1} = 1.355$ ($\phi_1 = 5.31$) which is close to the experimental value^{9,15} at which the state $|1\rangle$ efficiently tunnels out. [Recall that parameters of both qubits are given by Eq. (3).] The corresponding WKB tunneling rate^{16,17} for the state $|1\rangle$ is 3×10^9 s⁻¹, which ensures tunneling during few-nanosecond-long measurement pulse as in experiments of Refs. 6 and 9. Notice that the barrier height N_{l1} is smaller than the naive estimate 1.5 for the dimensionless energy of the state $|1\rangle$. Actually, because of significant anharmonicity, the energies of states $|0\rangle$ and $|1\rangle$ in this case are 0.475 and 1.26 from the well bottom in units of $\hbar\omega_{l1}$, where $\omega_{l1}/2\pi = 6.87$ GHz. We neglect the fact that in the experiment the biasing of the first qubit returns back to $N_{l1} \sim 5$ after the measurement pulse; as

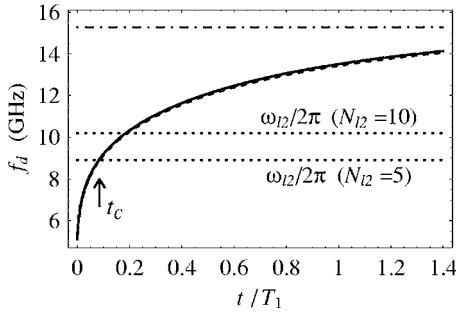


FIG. 4. The first-qubit oscillation frequency f_d as a function of time t (normalized by the energy relaxation time T_1) for $C_x=0$ (solid line) and $C_x=6$ fF (dashed line), assuming $N_{11}=1.355$ and parameters of Eq. (3). Dash-dotted horizontal line, $\omega_{r1}/2\pi = 15.3$ GHz, shows the long-time limit of $f_d(t)$. Two dotted horizontal lines show the plasma frequency for the second qubit: $\omega_{l2}/2\pi = 10.2$ GHz for $N_{l2}=10$ and $\omega_{l2}/2\pi = 8.91$ GHz for $N_{l2}=5$. The arrow shows the moment t_c of exact resonance in the case $N_{l2}=5$.

we checked, this does not lead to a significant change of the evolution dynamics in the right well.

At the initial moment $t=0$ the first qubit is assumed to be in the right well close to the barrier top position, with the velocity $\dot{\delta}_1=0$. However, instead of assuming its initial energy to be the same as the energy of state $|1\rangle$, we choose a slightly lower energy, which is below the top of the barrier by 20% of the well depth ΔU_{l1} . This (somewhat arbitrary) choice prevents unphysically slow dynamics of a classical particle in the case when it is very close to the barrier top (quantum dynamics due to dissipation does not significantly slow down at the energy close to the barrier top). We have also checked that the qubit dynamics is not too sensitive to the choice of initial energy (when it is above the left well bottom and not too close to the barrier top).

Since the initial energy of the first qubit (with respect to the bottom of the right well) is much higher than the maximal energy of the second qubit in the left well, one can neglect the back action from the second qubit while it remains in the left well. Then a one-qubit approach can be used for the dynamics of the first qubit (see details in Appendix C):

$$\ddot{\delta}_1 + \frac{\dot{\delta}_1}{(1+\zeta)CR} + \frac{2\pi I_0}{\Phi_0 C(1+\zeta)} \sin \delta_1 + \frac{\delta_1 - \phi_1}{(1+\zeta)CL} = 0, \quad (9)$$

that shows damped oscillations in the right well. It is very important to notice that due to anharmonicity of the potential, the gradual decrease of the qubit energy leads to the gradual increase in time of the first-qubit oscillation frequency f_d (which drives the second qubit).⁹

The time dependence $f_d(t)$ of the oscillation frequency is shown in Fig. 4 for $C_x=0$ (solid line) and 6 fF (dashed line) assuming $T_1=25$ ns. The curves are very close to each other showing very small effect of the effective mass (capacitance) renormalization ($m \rightarrow m''$; see Appendix B). We have also checked numerically that variation of T_1 from

25 ns to 500 ns does not change noticeably the dependence $f_d(t)$ if the time is normalized by T_1 , which is rather obvious since $f_d \gg T_1^{-1}$.

Figure 4 shows that the oscillation frequency sharply increases initially and then slowly tends to the right-well plasma frequency $\omega_{r1}/2\pi = 15.3$ GHz (the dash-dotted horizontal line in Fig. 4). This is explained by the fact that the initial system energy is close to the barrier top, where the oscillation frequency is significantly lower (it tends to zero when the energy approaches the barrier top), while anharmonicity becomes relatively weak after the energy is no longer close to the barrier top.

Notice that it takes a finite time t_c for the first qubit dynamics to get into resonance with the second qubit ($\omega_{l2}/2\pi$ is around 9–10 GHz, as mentioned above); we find from Fig. 4 that $t_c = 0.085T_1$ for $N_{l2}=5$ and $t_c = 0.192T_1$ for $N_{l2}=10$. As a simple estimate, this is the time after which the second qubit becomes significantly excited.⁹ [Delay time t_c increases with N_{l2} because of ω_{l2} increase: $\omega_{l2} \propto N_{l2}^{1/5}$, as follows from Eqs. (A13) and (A15).]

IV. SECOND QUBIT: CLASSICAL APPROACH

Before considering quantum dynamics of the second qubit (see next section), let us first discuss its classical dynamics; this will give an insight useful for understanding the quantum results. The classical dynamics can be described by the equation (see discussion in Appendix D)

$$\ddot{\delta}_2 + \frac{\dot{\delta}_2}{(1+\zeta)T_1'} + \frac{2\pi I_0}{\Phi_0 C(1+\zeta)} \sin \delta_2 + \frac{\delta_2 - \phi_2}{(1+\zeta)CL} = \zeta \ddot{\delta}_1(t), \quad (10)$$

in which the oscillating driving force $\zeta \ddot{\delta}_1(t)$ has a slowly varying period and amplitude. Notice that we will often neglect the energy relaxation in the second qubit ($T_1' = \infty$). Besides being a simplifying assumption, this may be really relevant to the experimental situation because recent experimental data¹⁸ indicate that in long- T_1 qubits effective relaxation time in the deep right well may be significantly shorter than T_1 in the shallow left well.

A. Harmonic-oscillator model

Though Eq. (10) is simpler than the exact equation (5), its solution is still complicated and generally chaotic.¹⁹ Further simplification can be obtained by using the model of an undamped harmonic oscillator for the second qubit:⁹

$$\ddot{x} + \omega_{l2}^2 x = \zeta \ddot{\delta}_1(t), \quad (11)$$

where $x = \delta_2 - \delta_{l2}$, δ_{l2} is the left-well minimum position, and ω_{l2} is the unperturbed plasma frequency (see Appendix D). Correspondingly, the oscillator energy is $E_2 = m(\dot{x}^2 + \omega_{l2}^2 x^2)/2$, which can be calculated as²⁰

$$E_2(t) = \frac{\zeta^2 m}{2} \left| \int_0^t dt' e^{-i\omega_{l2}t'} \dot{\delta}_1(t') \right|^2, \quad (12)$$

assuming that the system is initially at rest at the potential minimum, $x(0) = \dot{x}(0) = 0$.

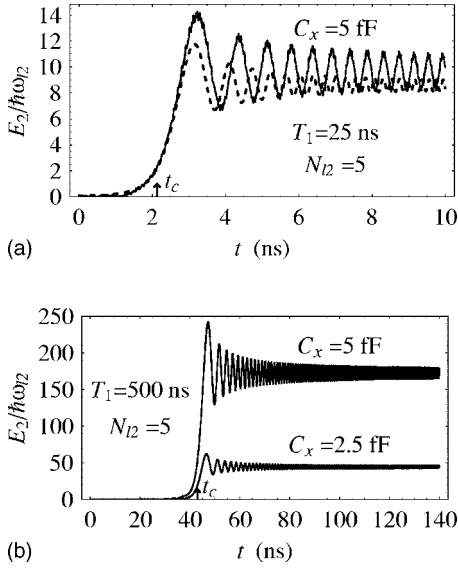


FIG. 5. The second qubit energy E_2 (in units of $\hbar\omega_{l2}$) in the oscillator model as a function of time t (in ns) for (a) $C_x=5$ fF and $T_1=25$ ns and (b) $C_x=2.5$ fF and 5 fF and $T_1=500$ ns, while $N_{l2}=5$. Dashed line in (a) shows analytical approximation using Eq. (D3). The arrows show the moment t_c when the driving frequency f_d (see Fig. 4) is in resonance with $\omega_{l2}/2\pi=8.91$ GHz.

Figure 5 shows the time dependence of the energy $E_2(t)$ in units of $\hbar\omega_{l2}$ for $\omega_{l2}/2\pi=8.91$ GHz, which corresponds to $N_{l2}=5$ (parameters of the first qubit evolution have been discussed in Sec. III and correspond to Fig. 4). One can see that the energy E_2 remains very low until a sharp increase followed by gradually decreasing oscillations. This behavior can be easily explained by changing in time frequency $\omega_d=2\pi f_d$ of the driving force (Fig. 4) which passes through the resonance⁹ with the second qubit frequency ω_{l2} at $t=t_c$.

An analytical analysis of the frequency crossing (see Appendix D) gives the approximate result (D3) for the dependence $E_2(t)$, shown by the dashed line in Fig. 5(a). The corresponding maximum energy is

$$E_{2,\max} = \frac{1.37\pi\zeta^2 mA^2}{\alpha}, \quad (13)$$

where $\alpha=d\omega_d/dt$ is the frequency sweep rate at the crossing point $t=t_c$, and A is the half-amplitude of $\delta_1(t)$ oscillations at $t=t_c$. The result (13) can be understood in the following way. In the case of exact resonance, the oscillation amplitude of $x(t)$ in Eq. (11) increases linearly in time with the rate²⁰ $\zeta A/\omega_{l2}$. The effective time of resonance Δt corresponds to a significant phase shift due to beating: $\alpha(\Delta t)^2 \sim 1$. Therefore the resulting amplitude after the resonance crossing is $\sim \zeta A/\omega_{l2}\sqrt{\alpha}$ and the corresponding energy is $E_2 \sim \zeta^2 mA^2/\alpha$, which coincides with Eq. (13) up to a numerical factor. A noticeable difference between numerical and analytical results in Fig. 5(a) is because the parameters A and α actually change with time, in contrast to the assumption used for analytics.

So far we have completely neglected the energy relaxation in the second qubit. Since the effective time of reso-

nance is $\Delta t \sim 3/\sqrt{\alpha}$ [rise time of the function $F(\bar{t})$ in Eq. (D3) from the 10% level to the maximum], the neglected effect should not be important (less than $\sim 10\%$) for $T_1 \gtrsim 30/\sqrt{\alpha}$. Using the estimate $\alpha=110 \text{ ns}^{-1}/T_1$ (see Fig. 4 and Appendix D), we find that taking into account the second qubit relaxation would not change significantly our results for $E_{2,\max}$ if $T_1 \gtrsim 10$ ns, which justifies our model.

Let us discuss the dependence of the maximum energy $E_{2,\max}$ of the second qubit on C_x and T_1 . Taking into account that $\zeta \propto C_x$ (for $C_x \ll C$) and $\alpha \propto 1/T_1$, we obtain from Eq. (13) the scaling

$$E_{2,\max} \propto C_x^2 T_1. \quad (14)$$

As seen from Fig. 5, numerical results confirm the obvious scaling $E_{2,\max} \propto C_x^2$, while the scaling $E_{2,\max} \propto T_1$ is not very accurate, but is still good as a first approximation.

In this subsection we have treated the second qubit as a harmonic oscillator. However, to analyze the measurement error due to the crosstalk, we have to assume switching from the left well to the right well when $E_{2,\max} > N_{l2}\hbar\omega_{l2}$ (which is surely not fully consistent with the oscillator model). All curves in Fig. 5 ($N_{l2}=5$) correspond to such switching, leading to the measurement error. The measurement error can be improved by decreasing the coupling capacitance C_x , which should be chosen to be smaller for larger T_1 . Equation (14) implies that to avoid the errors due to crosstalk, one needs to choose

$$C_x < C_{x,T} = B/\sqrt{T_1}, \quad (15)$$

where $C_{x,T}$ is the threshold coupling capacitance. From the numerical simulations (see Fig. 5) we obtain $B \approx 15 \text{ fF}\sqrt{\text{ns}}$ in the case $N_{l2}=5$. For $N_{l2}=10$ we get $B \approx 14 \text{ fF}\sqrt{\text{ns}}$. Notice that for experimental parameters of Ref. 9 ($C_x=6 \text{ fF}$, $T_1=25 \text{ ns}$) this bound is exceeded approximately twice, which is an indication that our simple model is not sufficiently accurate. As we will see in the next subsection, the theoretical bound is softer (higher) when we use actual potential profile for the second qubit instead of using the harmonic oscillator model.

B. Actual qubit potential

Let us analyze the second qubit evolution still using the classical model, but taking into account the actual potential profile $U_2(\delta_2)$, i.e., solving Eq. (10) instead of the simplified equation (11). Figures 6 and 7 show the time dependence of the second-qubit energy,

$$E_2 = (1 + \zeta)m\dot{\delta}_2^2/2 + U_2(\delta_2), \quad (16)$$

in the absence of dissipation in the second qubit ($T_1'=\infty$) for $N_{l2}=5$ and 10, while $T_1=25$ ns. [In this subsection we take into account the mass renormalization $m \rightarrow m''=(1+\zeta)m$ explicitly (see Appendix B), even though this does not lead to a noticeable change of results.] A comparison of Figs. 5(a) and 6 shows that in both models the qubit energy remains small before a sharp increase in energy. However, there are significant differences due to account of anharmonicity: (a) The sharp energy increase occurs earlier than in the oscillator model (the position of short-time energy maximum is shifted

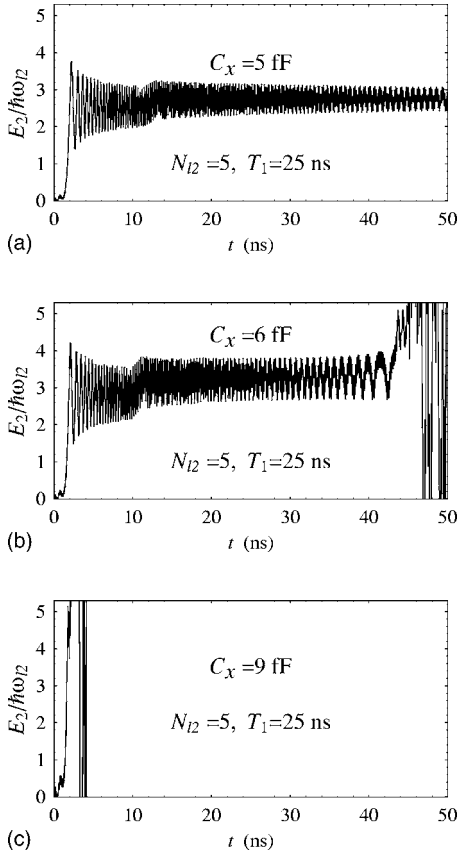


FIG. 6. The second-qubit energy E_2 (in units of $\hbar\omega_{l2}$) as a function of time t (in ns) for $N_{l2}=5$, $T_1=25$ ns, and (a) $C_x=5$ fF, (b) $C_x=6$ fF, and (c) $C_x=9$ fF. The classical model with actual qubit potential is used; energy relaxation in the second qubit is neglected, $T_1'=\infty$. In (b) and (c) the qubit switches (goes over the barrier) at 44 ns and 2.1 ns, respectively.

approximately from 3 ns to 2 ns); (b) The excitation of the qubit may be to a much lower energy than for the oscillator; (c) After the sharp increase, the energy occasionally undergoes noticeable upward (as well as downward) jumps, which may overshoot the initial energy maximum; (d) The model now explicitly describes the qubit escape (switching) to the right well [Figs. 6(b) and 6(c)]; in contrast to the oscillator model, the escape may happen much later than initial energy increase; for example, in Fig. 6(b) the escape happens at $t \approx 44$ ns $\gg t_c \approx 2.1$ ns.

The properties (a) and (b) can be understood by taking into account the fact that the oscillation frequency in the

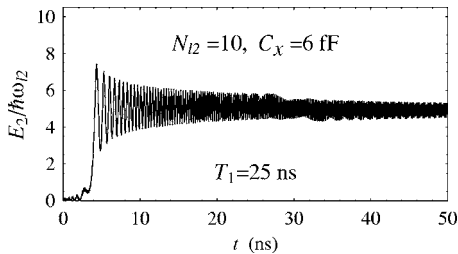


FIG. 7. Same as in Fig. 6 for $N_{l2}=10$, $T_1=25$ ns, and $C_x=6$ fF.

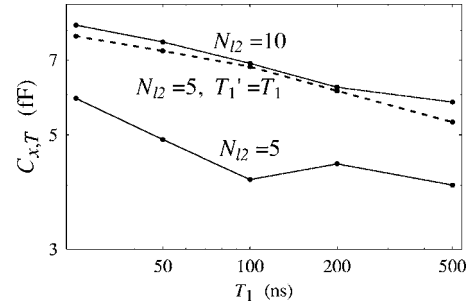


FIG. 8. The log-log plot of the threshold coupling capacitance $C_{x,T}$ vs T_1 in the classical model assuming $T_1'=\infty$ (solid lines) or $T_1'=T_1$ (dashed line) for $N_{l2}=5$ (dashed and lower solid line) and 10 (upper solid line). The crosstalk excitation does not switch the second qubit if $C_x < C_{x,T}$. The numerical data are shown by the dots; the lines are just guides for the eye.

second qubit *decreases* with the energy increase (it should become formally zero at the top of the barrier), while the driving frequency *increases* with time (Fig. 4). Therefore, initially small out-of-resonance beatings when $\omega_d < \omega_{l2}$ are amplified because of the positive feedback: larger amplitude makes it closer to the resonance, which increases the amplitude even more. This makes the nonexcited state unstable, which leads to a sharp increase of the qubit energy earlier than the condition $\omega_d = \omega_{l2}$ is satisfied. The same mechanism is also responsible for lower qubit excitation, when compared to the harmonic oscillator model: the resonance cannot be as efficient as in the harmonic oscillator model since the qubit excitation quickly moves the qubit frequency out of the resonance. The property (c) is related to crossing of higher-order resonances, which occur when $\omega_d(t)$ is commensurate²⁰ with the oscillation frequency of the system, which itself depends on the energy $E_2(t)$ and hence on the time. Similar mechanism is responsible for the qubit switching at $t \gg t_c$; in particular, in Fig. 6(b) the switching happens when the driving frequency ω_d becomes approximately twice larger than the second qubit frequency.

In contrast to the oscillator model, Eq. (10) for the actual qubit potential cannot be solved analytically,²¹ so we rely only on the numerical simulations. We are interested in the conditions, for which the system remains in the left well. Generally, the qubit excitation increases with increase of the coupling C_x ; therefore one expects a certain threshold value $C_{x,T}$ (depending on T_1 and other parameters), which separates the switching and no-switching scenarios. However, because of the complex dynamics of the system, the dependence on C_x is nonmonotonous, so that increasing C_x may sometimes change switching case into no-switching case. In this situation, we define $C_{x,T}$ as a minimum value at which the switching happens (even though larger C_x may correspond to no-switching). Similar to the harmonic oscillator model, we expect that $C_{x,T}$ generally decreases with increase of T_1 ; however, because of the complex dynamics, the dependence $C_{x,T}(T_1)$ should not necessarily be monotonous.

The dots connected by two solid lines in Fig. 8 show the numerically calculated $C_{x,T}$ for $N_{l2}=5$ and 10, for 5 values of T_1 ranging from 25 ns to 500 ns (so far we still assume $T_1'=\infty$). For these calculations we have used the increment of

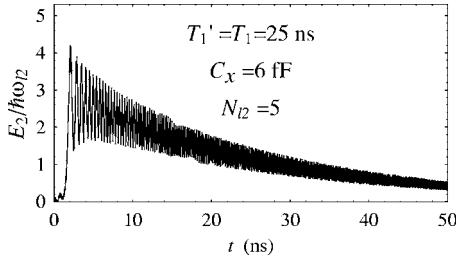


FIG. 9. The second-qubit energy $E_2(t)$ in the classical model taking into account energy dissipation in the second qubit, for $N_{l2} = 5$, $C_x = 6$ fF, and $T_1' = T_1 = 25$ ns. [Compare with Fig. 6(b).]

0.1 fF for C_x and simulated the qubit dynamics in the time interval $0 \leq t \leq 6T_1$. Notice that the lines are not smooth (the lower line even has a bump), which is the result of irregular nonlinear dynamics of the system. Nevertheless, the numerical results confirm the generally decreasing dependence $C_{x,T}(T_1)$, and fitting solid lines by the formula

$$C_{x,T}(T_1) \approx BT_1^{-\beta} \quad (17)$$

(where $C_{x,T}$ is measured in fF while T_1 is measured in ns) we obtain $B \approx 8$ and 12 for $N_{l2} = 5$ and 10, respectively, while $\beta \approx 0.12$ for the both lines.

Since the gate speed is proportional to C_x , it is advantageous to have higher C_x . The above results show that raising the barrier after the measurement pulse to $N_{l2} = 10$ would allow us to increase C_x in comparison with the case $N_{l2} = 5$. The reason for this can be understood by comparing Figs. 6(b) and 7, which show that in the case $N_{l2} = 10$ the sharp energy increase is lower relative to the barrier top than for $N_{l2} = 5$. Note that the dependence (17) is much weaker than the relation $C_{x,T} \propto T_1^{-1/2}$ obtained in the oscillator model, which is advantageous for design of qubits with weak decoherence (large T_1).

Now let us consider the effect of dissipation in the second qubit. The dashed line in Fig. 8 shows $C_{x,T}(T_1)$ dependence in the presence of dissipation (with $T_1' = T_1$) for the same other parameters as for the lower solid line (for which $T_1' = \infty$). As we see, account of dissipation increases $C_{x,T}$ quite noticeably, which contradicts the conclusion from the harmonic oscillator model (predicting no significant dependence). The reason is that for C_x slightly above $C_{x,T}$ the switching in the model without dissipation usually occurs significantly later than the initial sharp increase of the energy [see Fig. 6(b)] and is caused by “secondary” jumps of the energy due to strongly nonlinear dynamics, as discussed above. Dissipation in the second qubit (Fig. 9) shortens significantly the time interval during which the switching due to secondary jumps is possible, thus increasing $C_{x,T}$. (We would also like to mention a possibility of a system return into the left well after the escape into the right well, which may take place with or without dissipation.) Fitting the dashed line in Fig. 8 by the power-law dependence (17), we find $B \approx 12$ and $\beta \approx 0.13$, so that the scaling power β is practically the same as in the no-dissipation case, while B becomes considerably larger.

V. SECOND QUBIT: QUANTUM APPROACH

In the quantum approach we describe the second qubit by the wave function $\psi(\delta, t)$ (in this section we often omit the subscript 2 to shorten notations), which obeys the Schrödinger equation

$$i\hbar \frac{\partial \psi}{\partial t} = H_r(t) \psi \quad (18)$$

with the reduced one-qubit Hamiltonian (see derivation in Appendix E)

$$H_r(t) = H_0 + V(t), \quad H_0 = \frac{\hat{p}^2}{2m(1+\zeta)} + U(\delta) \quad (19)$$

$$V(t) = -\zeta(1+\zeta)m\ddot{\delta}_1(t)\delta. \quad (20)$$

This Hamiltonian exactly corresponds to the classical model used in the previous section. Similarly to the classical case (Appendix D), the difference between $\zeta(1+\zeta)m$ and $m_x = (\Phi_0/2\pi)^2 C_x$ in the formula for $V(t)$ should not be taken seriously, as being within the accuracy of treating two qubits separately (same applies in general to the difference between the renormalization factor $1+\zeta$ and $1+C_x/C$).

The second-qubit wave function ψ is expanded over the (time-independent) eigenfunctions ψ_n of H_0 ,

$$\psi(\delta, t) = \sum_n a_n(t) \psi_n(\delta), \quad (21)$$

and the evolution of the occupation amplitudes a_n is calculated using the method described in Appendix E.

We define the probability $P_l(t)$ to find the second qubit in the left well as

$$P_l(t) = \sum_{n_k} P_{n_k}(t), \quad P_n(t) = |a_n(t)|^2, \quad (22)$$

where $P_n(t)$ is the probability of state n occupation, and the summation is only over the states localized in the left well. We will also denote $P_{n_k}(t)$ as $Q_k(t)$, where k enumerates the states in the left well, starting from $k=0$ (the left-well ground state). We define the switching probability as $P_s(t) = 1 - P_l(t)$. Notice that we consider transition to delocalized states (above the barrier) as escape from the left well (even though in this case there is a possibility of “repopulation” of the left well if dissipation is taken into account).

Figure 10 shows (for the case $N_{l2} = 10$) the eigenfunctions $|\psi_n(\delta)|^2$ and the corresponding energies E_n for $145 \leq n \leq 171$, where the level numbering starts with $n=0$ for the ground state (in the right well). One can distinguish 3 types of states: (a) 12 states localized in the left well ($n = 146, 148, \dots, 166, 169$ or, respectively, $k=0, \dots, 11$), (b) delocalized states ($n \geq 170$), and (c) states localized in the right well (the remaining states). Depending on the barrier height N_{l2} (controlled by the external flux ϕ_2), the resonant states may also be present: when the energies of states localized in the left and right wells approach each other sufficiently close, the states mix and become delocalized. Actually, in Fig. 10 the left-well states $k=10$ and 11 are partially delocalized due to interaction (tunneling) with neighboring

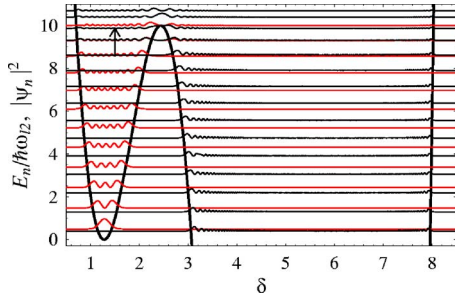


FIG. 10. (Color online) The second qubit potential $U(\delta)$ (thick line) and eigenfunctions $|\psi_n(\delta)|^2$ ($145 \leq n \leq 171$), shifted vertically by the energy eigenvalues E_n (in units of $\hbar\omega_{12}$) for $N_{l2}=10$ and $C_x=6$ fF ($\omega_{l2}/2\pi=10.2$ GHz). The energy origin is chosen at the minimum of the left well. An arbitrary scale for $|\psi_n|^2$ is chosen to be $1/8$ of the $E_n/\hbar\omega_{12}$ scale. The arrow illustrates the dominating transition responsible for the escape from the level $k=9$ at $t \approx 16$ ns.

right-well states. Notice that even though the left-well energies are practically insensitive to the coupling capacitance C_x ($C_x=6$ fF for Fig. 10), their relative energy shift with the right-well level comb depends on C_x significantly because the right well is very deep, $n \geq 10^2$.

Figure 11 shows the left-well population $P_l(t)$ for $N_{l2}=10$ and $T_1=25$ ns (energy dissipation in the second qubit is neglected, $T_1'=\infty$). Figure 12 shows the populations of the first 10 levels in the left well; the populations of levels $k=10$ and 11 are not shown since they are very close to zero.

Figure 13 shows the time dependence of the qubit mean energy

$$\langle E(t) \rangle = \sum_n E_n P_n(t) \quad (23)$$

for the same parameters as in Figs. 11 and 12. Comparing the mean energy with the classical qubit energy for the same parameters (Fig. 7), we see that the two curves are similar, though classical energy shows larger fluctuations. Note that the mean energy starts at $t=0$ from a nonzero value equal to the qubit energy in the ground state $\approx \hbar\omega_{l2}/2$. Even though the mean energy is significantly lower than the barrier height (similar to the classical energy), the escape probability $P_s(t)=1-P_l(t)$ is nonzero in the quantum case (see Fig. 11).

The time dependence of the switching probability (Fig. 11) looks quite irregular. This shows that the quantum behav-

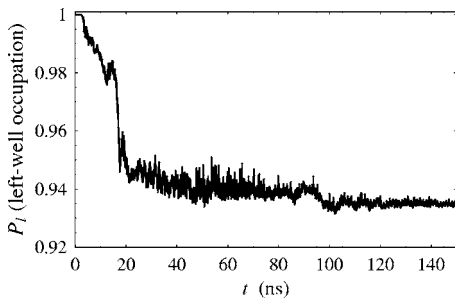


FIG. 11. The probability $P_l=1-P_s$ for the second qubit to remain in the left well as a function of time t for $N_{l2}=10$, $C_x=6$ fF, and $T_1=25$ ns.

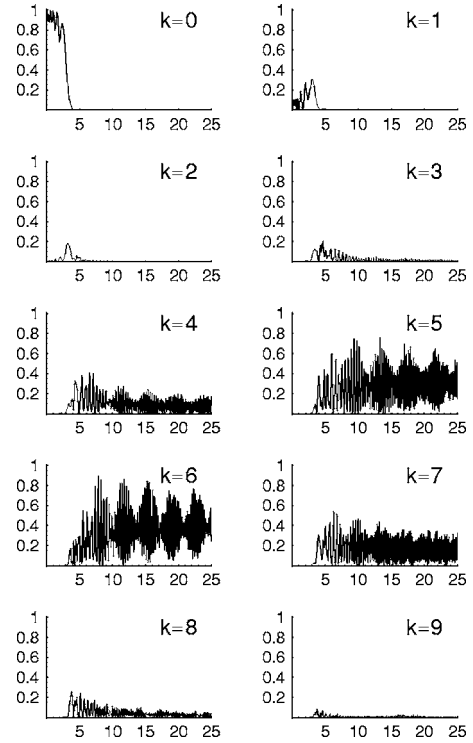


FIG. 12. The occupation probabilities $Q_k(t)$ for the left-well levels k as functions of time t (in ns) for $N_{l2}=10$, $C_x=6$ fF, and $T_1=25$ ns.

ior is rather complicated, similar to the classical behavior discussed in Sec. IV B. As seen in Figs. 12 and 13, at $t \lesssim 3$ ns, when the driving force is far from the resonance with the qubit, the population mainly remains in the ground state. At this stage, there is no switching (see Fig. 11). Similar to the classical case, there is a fast qubit excitation (though still almost without switching) between 3 ns and 4 ns (a little earlier than the moment $t_c=4.8$ ns of classical resonance), while the main switching happens much later, mostly at $t \approx 16$ ns.

To understand the excitation mechanism, we show in Fig. 14 the Rabi frequencies $R_{k,k-1}=2\zeta m'' A |\delta_{k,k-1}|/\hbar$ for the adjacent left-well transitions; $R_{k,k-1}$ is equal to the amplitude of $V_{k,k-1}(t)/\hbar$ oscillations [actually, since $V(t) \propto \ddot{\delta}_1(t)$ given by Eq. (20) is significantly nonharmonic in time, we need to use the amplitude of the resonant component]. Since the amplitude $2A(t)$ of $\ddot{\delta}_1$ oscillations (fundamental frequency compo-

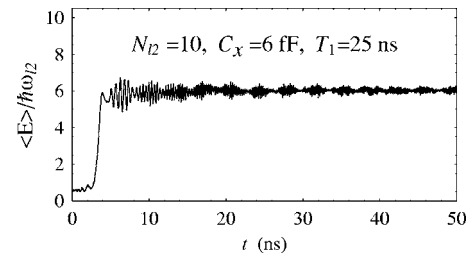


FIG. 13. Time dependence of the mean energy $\langle E \rangle$ of the second qubit [Eq. (23)] in units of $\hbar\omega_{12}$ for $N_{l2}=10$, $C_x=6$ fF, and $T_1=25$ ns.

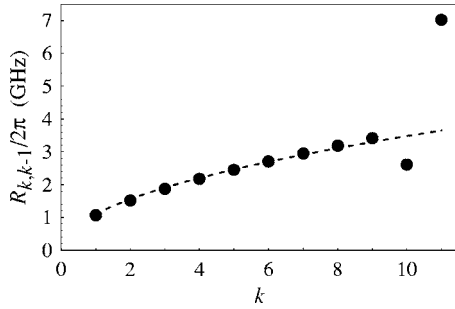


FIG. 14. Dots: Rabi frequencies $R_{k,k-1}/2\pi$ for the left-well transitions at $t=t_c$, for $N_{l2}=10$, $C_x=6$ fF, and $T_1=25$ ns. Dashed line shows analytical dependence $1.1\sqrt{k}$ GHz.

ment) changes with time (see Appendix D), the Rabi frequencies also change with time. In Fig. 14 we show the values corresponding to the exact classical resonance, $f_d(t_c) = \omega_{l2}/2\pi$, which happens at $t_c=4.8$ ns (then $A=5.2 \times 10^3$ ns $^{-2}$); for comparison, at $t \approx 3$ ns the value of A and, correspondingly, the Rabi frequencies are approximately 10% smaller. (Notice that the moment t_c scales with T_1 , but the values of Rabi frequencies at t_c do not change with T_1 .) For the levels not too close to the barrier top, one can use the harmonic-oscillator relation²³ $|\delta_{k,k-1}| \approx \sqrt{k\hbar}/2m''\omega_{l2} \approx 0.10\sqrt{k}$ [for $N_{l2}=10$ and parameters of Eq. (3)], yielding $R_{k,k-1}/2\pi \approx A(C_x/C)\sqrt{2km''/\hbar}\omega_{l2}/2\pi \approx 1.1\sqrt{k}$ GHz. This formula fits well the numerical results in Fig. 14 up to $k=9$; for higher levels anharmonicity becomes really strong.

Figure 15 shows the time dependence of the corresponding detunings $\omega_{k,k-1}/2\pi - f_d(t)$. Though the exact resonance with the transition $0 \leftrightarrow 1$ ($\omega_{10}/2\pi=10.0$ GHz) happens at $t=4.3$ ns, a significant excitation starts earlier, at $t \approx 3$ ns, when the detuning $\omega_{10}/2\pi - f_d(t)$ becomes less than the Rabi frequency $R_{10} \approx 1$ GHz. Since the Rabi frequency increases with k , while the detuning first decreases and then increases with k (after detuning changes sign), the ground level population rapidly propagates to higher levels, until the detuning becomes so large that the further excitation stops. As a result, at $t \geq 4$ ns the levels 0–2 become practically empty, while almost all the population is transferred to levels 4–7. Similar to the classical case, the excitation efficiency is significantly suppressed by the fact that driving frequency $f_d(t)$ increases with time, while the level spacing decreases with the level

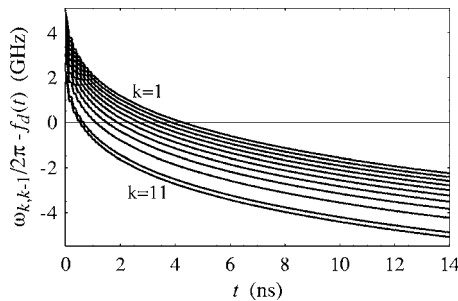


FIG. 15. Time dependence of the frequency detunings $[\omega_{k,k-1} - \omega_d(t)]/2\pi$ of left-well transitions $(k-1) \leftrightarrow k$ for $N_{l2}=10$, $C_x=6$ fF, and $T_1=25$ ns. Curves from top to bottom correspond to $k=1, 2, \dots, 11$.

number k . Therefore, by the time at which levels $k \geq 5$ become populated, the further up-transitions are already out of resonance (which happened for them earlier), becoming even farther off resonance with increasing time.

The escape (switching) in the quantum case can occur in several ways. The population which goes to the highest states $k=10$ and 11 is lost rather fast (within a fraction of nanosecond), since those states interact significantly with the right-well and delocalized states. However, in our simulation transitions for these states are quite weak because of significant detuning (even though the Rabi frequency is not much smaller than detuning, the level occupations above $k=7$ decrease 4–10 times per level, so the occupation of the level $k=10$ is already very small).

Another switching mechanism is the following. With the increase of the driving frequency $f_d(t)$, it can become resonant with transitions between nonadjacent states, thus populating the states close or above the barrier, which cannot be populated otherwise. In particular, more than half of the switching probability in Fig. 11 is due to the sharp decrease of $P_l(t)$ between 16 ns and 18 ns, which happens because of the transition between the state $k=9$ ($n=164$) and the right-well state $n=168$ with the difference frequency of 13.2 GHz (see the arrow in Fig. 10). At $t=16$ ns the detuning for this transition is 0.7 GHz ($f_d=12.5$ GHz), which is much smaller than other detunings between the levels of interest and is comparable to the corresponding Rabi frequency ≈ 0.5 GHz. This value of the Rabi frequency is obtained as above, taking into account the matrix element $|\delta_{164,168}|=0.048$ and the value $A=5.8 \times 10^3$ ns $^{-2}$ at $t=16$ ns.

Notice that in our numerical method the wave function is represented in the basis of nonperturbed (time-independent) eigenstates. An alternative way would be to diagonalize the Hamiltonian at each moment of time and use the time-dependent eigenstates. Even though both methods are formally equivalent, the second method would be more natural to use if the dissipation is taken into account. In the time-dependent language an important mechanism of escape is Landau-Zener tunneling through the barrier. The perturbation $V(t)$ in the Hamiltonian (20) is equivalent to changing in time magnetic flux,

$$\phi_2 \rightarrow \phi_2 + \zeta(1 + \zeta)LC\ddot{\delta}_1(t), \quad (24)$$

which changes N_{l2} and leads to oscillations of the energy shift between the comb of levels in the left well and the right-well comb. Because of rather strong amplitude of these oscillations (in the example of Figs. 11–15, N_{l2} oscillates between 9.15 to 11.2), each left-well level crosses with several right-well levels during one oscillation cycle. These (avoided) crossings lead to transitions between the states in different wells (tunneling), the rate of which, according to the Landau-Zener formula,²³ is $\propto W^2$, where W is the minimal level splitting at the crossing. The values of W increase exponentially with increase of k . Therefore, the Landau-Zener tunneling is a relatively slow (ineffective) switching mechanism for all levels, except for the highest ones (such as $k=10$ and 11). Besides the Landau-Zener mechanism, the escape from the left well may also happen because the upper

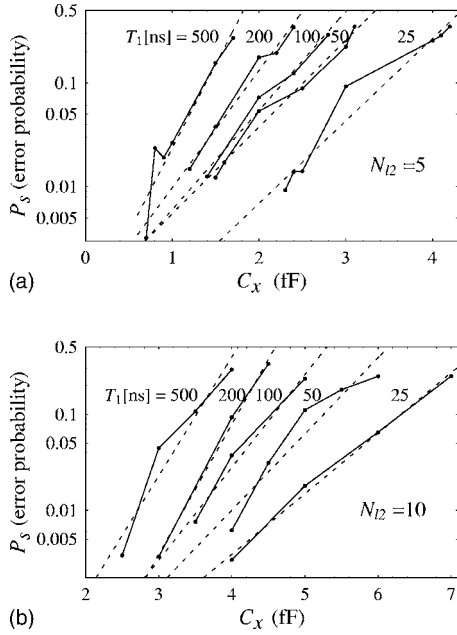


FIG. 16. The qubit switching (error) probability P_s as a function of coupling capacitance C_x (in fF) for $T_1=25, 50, 100, 200,$ and 500 ns for (a) $N_{l2}=5$ and (b) $N_{l2}=10$. The numerical data are represented by points, connected by solid lines as guides for the eye. The dashed straight lines are results of the least-squares fit (notice the logarithmic scale).

left-well states may become delocalized (above the barrier) when the barrier N_{l2} decreases in the process of oscillations. We would also like to mention that the oscillations of $\ddot{\delta}_1$ (and therefore of N_{l2}) are strongly nonharmonic. In particular, the mentioned above range $9.15 < N_{l2} < 11.2$ remains constant during long time interval $0 < t < 0.4T_1$, because these extrema actually do not correspond to the turning points of $\delta_1(t)$ oscillations; instead, they correspond to the points of inflection δ'_c and $\delta_c + 2\pi$ of $U(x)$ [see Eq. (A5)], as long as these points are within the oscillation swing of $\delta_1(t)$.

We have performed extensive calculations of the switching probability $P_s(t)$, varying the parameters $C_x, T_1,$ and N_{l2} . We run simulations within the time interval $[0, 6T_1]$; after $6T_1$ the first-qubit oscillations decay to a very low level, so the perturbation of the second qubit is weak, and the further change of $P_s(t)$ is practically negligible. Correspondingly, we define the total switching probability P_s (which is the crosstalk error probability) as $P_s(6T_1)$.

The results of numerical calculation of $P_s(C_x)$ dependence for several values of T_1 and two values of N_{l2} (5 and 10) are shown in Fig. 16. Notice that the lines connecting the data points are not smooth and sometimes are even nonmonotonic. This may be explained by complicated dynamics, similar to the irregular behavior in the classical case. Despite the $P_s(C_x)$ dependence in Fig. 16 is not smooth, we still see that the switching probability P_s decreases approximately exponentially with decrease of C_x .

Using the linear (on the semilog scale) least-square fit for the results shown in Fig. 16 (see dashed lines), we obtain the contour plots for P_s on the plane of C_x and T_1 (see solid lines in Fig. 17). The data in Fig. 17 can be fitted by straight lines,

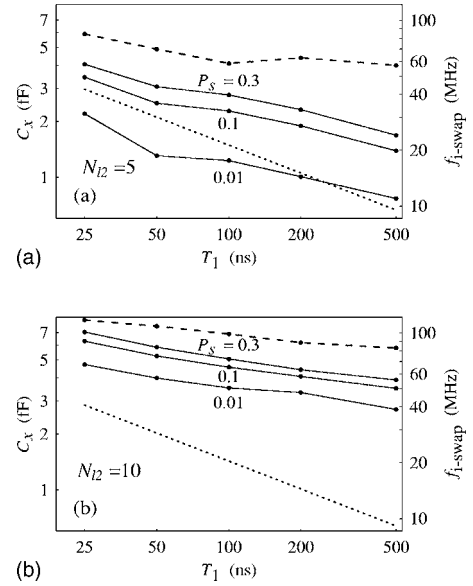


FIG. 17. Solid lines: log-log contour plots for the values of the error (switching) probability $P_s=0.01, 0.1,$ and 0.3 on the plane of relaxation time T_1 (in ns) and coupling capacitance C_x (in fF) in the quantum model for (a) $N_{l2}=5$ and (b) $N_{l2}=10$. The corresponding results for $C_{x,T}(T_1)$ in the classical models are shown by the dashed lines (actual potential model) and the dotted lines [oscillator model, Eq. (15)]. The numerical data are represented by the points, connected by lines as guides for the eye. The scale at the right corresponds to the operation frequency of the two-qubit imaginary-swap⁹ quantum gate.

yielding approximate power-law dependence [similar to Eq. (17)] for the threshold coupling capacitance $C_{x,T}$:

$$C_{x,T}(T_1) \approx B(P_s)T_1^{-\beta(P_s)}, \quad (25)$$

which now depends on the tolerable level P_s of the measurement error probability. The obtained numerical values of the parameters B and β in this formula are shown in Table I. Notice that β depends on P_s quite weakly, but decreases appreciably when N_l changes from 5 to 10. The values of β in Table I are greater than the value $\beta=0.12$ obtained in the classical model with actual qubit potential (Sec. IV B), but less than the value $\beta=0.5$ in the oscillator model [Eq. (15)]. This means that dependence on T_1 in Eq. (25) in the quantum model is in-between those found in the oscillator and actual-potential classical approaches. Figure 17 also shows a comparison between the results of classical and quantum ap-

TABLE I. Parameters of Eq. (25) for the quantum model (C_x is in fF and T_1 is in ns), limiting the coupling capacitance C_x for several values of the error probability P_s and dimensionless barrier height N_{l2} .

N_{l2}	5			10		
P_s	0.01	0.1	0.3	0.01	0.1	0.3
B	5.4	8.3	9.7	8.1	11	13
β	0.32	0.29	0.28	0.18	0.19	0.20

proaches. As one can see, both the oscillator (dotted line) and actual-potential (dashed line) classical models give the limits for C_x roughly similar to the quantum results (within a factor of ~ 2), with the exception of the case of the oscillator model for $N_l=10$ and $T_1 > 100$ ns. The value of the coupling capacitance C_x determines the speed of two-qubit quantum gates. The right scale of the vertical axis in Fig. 17 converts C_x into the operation frequency $f_{i\text{-swap}}=(C_x/C)\omega_{10}/2\pi$ of the imaginary-swap⁹ gate.

These results can be used for the design of phase-qubit-based quantum gates. In particular, they give us the maximum allowed coupling capacitance C_x and hence the maximum gate operation speed, for a particular tolerable value P_s of the error due to crosstalk. An important result of the quantum treatment is the exponential dependence of the error probability on C_x and a rather slow dependence on T_1 . This shows that the measurement crosstalk is not a significant roadblock for the fabrication of phase-qubit-based quantum gates with low decoherence and a sufficiently high operation speed.

The present quantum theory does not take into account dissipation in the second qubit. The dissipation shortens the effective crosstalk time and thus decreases the crosstalk error (the switching probability), similar to the classical case discussed in Sec. IV B. Thus, the present results give a lower bound for the maximum allowed C_x . Taking into account the results of the classical model, one may expect $\sim 30\%$ larger limit for the coupling capacitance (and two-qubit gate frequency) for a quantum model with the same energy dissipation in the second qubit as in the first qubit ($T'_1=T_1$).

VI. CONCLUSIONS

The main goal of this paper has been to study the crosstalk between two capacitively coupled flux-biased phase qubits after the measurement pulse. The first qubit, which escapes (switches) from the left to the right well during the pulse, has been modeled classically. The first qubit performs damped oscillations (with energy relaxation time T_1) with frequency $f_d(t)$ increasing in time, these oscillations perturb the capacitively coupled second qubit. The dynamics of the second qubit (which is initially in the ground state) has been treated both classically and quantum mechanically.

In the classical treatment of the second qubit, we have compared the previously suggested⁹ oscillator model, which allows for both analytical and numerical analysis, with the model based on the exact potential, which can be solved only numerically. Both models show a sharp resonant excitation of the second qubit. Though there is a certain similarity between the two models, they significantly differ both quantitatively and qualitatively. In contrast to the oscillator model, the exact-potential model shows nonlinear and irregular dynamics. The second qubit remains in the left well when the coupling capacitance is sufficiently low, $C_x \leq C_{x,T}$, but may escape (though not certainly because of complicated dynamics) if $C_x > C_{x,T}$. We have obtained numerically the dependence $C_{x,T}(T_1)$ both in the absence and presence of dissipation in the second qubit for experimentally relevant values of the barrier height.

For the quantum treatment we have developed an efficient numerical scheme, which uses a subset of eigenstates of the unperturbed Hamiltonian. In this case, similarly to the classical case, a fast excitation of the second qubit occurs at a moment when the driving frequency $f_d(t)$ is somewhat below the transition frequency between the ground and first excited states. However, in contrast to the classical case, the switching can now happen even when the qubit mean energy is significantly lower than the barrier height, either due to tunneling or due to excitation above the barrier.

The results for the switching (error) probability P_s have been presented as contour plots on the plane of coupling capacitance C_x and relaxation time T_1 (Fig. 17). Such plots may be important for the design of quantum gates based on phase qubits. Comparison of the results obtained in the quantum and classical models shows that the classical models can be used for a crude estimate of the crosstalk error; however, the difference becomes significant for $T_1 \gtrsim 100$ ns. In the quantum approach the dissipation in the second qubit have been neglected. However, by analogy with the classical case, one can expect that the account of dissipation will not change the results significantly, though it will somewhat increase the upper bound for the coupling capacitance, above which the crosstalk error becomes intolerable.

Recent experimental data¹⁸ give an indication that effective relaxation time T_1 in the deep right well may be somewhat shorter than the relaxation time in the shallow left well. Although not presently understood, in this case we should use the shorter right-well value of T_1 in our results. This is a favorable situation for experiments with quantum gates, since the measurement crosstalk is reduced by the shorter T_1 after switching (see Fig. 17), while the qubit coherence is governed by the normal (longer) T_1 . Even without this effect, our results show that the measurement crosstalk is not a significant problem for phase-qubit-based quantum gates with low decoherence and high operation speed, so the considered measurement scheme is suitable for a scalable quantum computer.

The model analyzed in this paper assumes fixed coupling between the qubits. Future implementations of experimental schemes with adjustable coupling (which can be practically zeroed at the time of measurement) will significantly suppress the crosstalk error mechanism and correspondingly allow for a significant increase in the operation frequency of the two-qubit quantum gates.

The present study can also be of relevance for problems in other fields (e.g., laser chemistry), which consider excitation or escape from a potential well by an oscillating driving force with parameters changing in time.

ACKNOWLEDGMENTS

The work was supported by NSA and DTO under ARO Grant No. W911NF-04-1-0204.

APPENDIX A: ONE-QUBIT POTENTIAL

In this Appendix we review the basic properties¹³ (see also Ref. 7) of the one-qubit potential energy $U(\delta)=E_J[\delta$

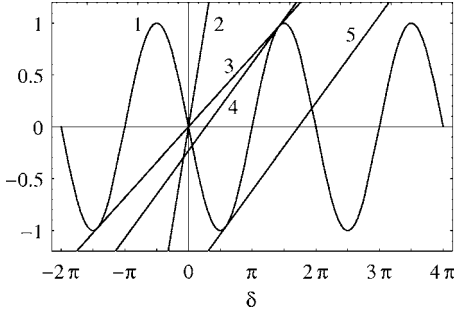


FIG. 18. The graphical solution of Eq. (A1); see text.

$-\phi)^2/2\lambda - \cos \delta]$ [see Eq. (2) and Figs. 1 and 3].

Since this potential is invariant with respect to the simultaneous change of δ and ϕ by $2\pi n$ where n is integer, we limit ourselves by the range $0 \leq \phi \leq 2\pi$ for the external flux. Notice that the potential is symmetric for $\phi = n\pi$ ($\Phi = n\Phi_0/2$).

The maxima and minima of the potential (2) satisfy the equation

$$(\delta - \phi)/\lambda = -\sin \delta, \quad (\text{A1})$$

which can be solved graphically. Figure 18 shows the right-hand side (r.h.s.) of Eq. (A1) (curve 1) and the l.h.s. (straight lines 2–5) for several values of the parameters. This equation can have only one solution when the straight-line slope is greater than 1 (as for line 2 in Fig. 18); therefore in the case $\lambda < 1$ the potential (2) has only one well for any external flux ϕ .

For $\lambda > 1$ the potential may have more than one well. There will be at most two wells if the slope of the l.h.s. of Eq. (A1) is greater than the slope $1/\lambda_1$ of the line 3 in Fig. 18, which is tangent to $-\sin \delta$ at two points $\pm\delta'$ (the line passes through the origin because of the symmetry). This condition yields the equation $\tan \delta' = \delta'$ with the least positive root $\delta'_1 = 4.493$, which corresponds to $\lambda_1 = -1/\cos \delta'_1 = 4.603$. Thus, for λ in the interval¹³

$$1 < \lambda < 4.603 \quad (\text{A2})$$

the potential has one or two wells, depending on ϕ . In particular, for the experimental parameters of Ref. 9 used in this paper [see Eq. (3)] one obtains $\lambda = 3.72$ (as for lines 4 and 5 in Fig. 18), which satisfies condition (A2). Similarly, one can show that the potential will have n or $n+1$ wells (depending on ϕ) if

$$\lambda_{n-1} < \lambda < \lambda_n \quad (n \geq 1), \quad (\text{A3})$$

where $\lambda_0 = 1$, $\lambda_n = 1/|\cos \delta'_n|$, and δ'_n is the n th (in the increasing order) positive root of the equation $\tan \delta' = \delta'$. In particular, $\lambda_2 = 7.790$, $\lambda_3 = 10.95$, $\lambda_4 = 14.10$, and $\lambda_n \approx (n+1/2)\pi$ for $n \geq 1$.

The condition for a two-well potential in the case (A2) can be found by considering the transition between the one-well and two-well cases, which is illustrated by lines 4 and 5 in Fig. 18. These lines are tangent to $-\sin \delta$ at the points δ_c , which correspond to the inflection points of the potential (2) (when a well disappears, the corresponding maximum and

minimum of the potential merge, so that both the first and second derivatives are zero at this point). Solving the equation for the inflection points

$$\cos \delta_c = -1/\lambda \quad (\text{A4})$$

(which does not depend on the external flux), we get two solutions in the interval $(0, 2\pi)$:

$$\delta_c = \pi/2 + \arcsin(1/\lambda), \quad \delta'_c = 2\pi - \delta_c. \quad (\text{A5})$$

Inserting these results into Eq. (A1), we finally obtain the condition for a two-well potential:

$$\phi'_c < \phi < \phi_c, \quad (\text{A6})$$

where the critical fluxes are

$$\phi_c = \pi/2 + \sqrt{\lambda^2 - 1} + \arcsin(1/\lambda), \quad \phi'_c = 2\pi - \phi_c \quad (\text{A7})$$

(it is easy to show that $\phi'_c < \phi_c$ for $\lambda > 1$).

The two wells have minima at $\delta = \delta_{l,r}$, which can be found from Eq. (A1). The corresponding “plasma” frequencies (the classical oscillation frequency near the well bottom) are

$$\omega_{l,r} = \sqrt{E_J(1/\lambda + \cos \delta_{l,r})/m}. \quad (\text{A8})$$

Cubic potential approximation

When one of the wells is very shallow, it can be approximated by a cubic potential.¹³ Assuming $0 < \phi_c - \phi \ll \phi_c$ (shallow left well) we can approximate $\cos \delta$ in the vicinity of inflection point δ_c [see Eq. (A4)] as

$$\begin{aligned} \cos \delta &= \cos \delta_c \cos y - \sin \delta_c \sin y \approx -\lambda^{-1}(1 - y^2/2 + y^4/24) \\ &\quad - \sqrt{1 - \lambda^{-2}}(y - y^3/6), \end{aligned} \quad (\text{A9})$$

where $y = \delta - \delta_c$ (in the following the term y^4 is neglected; it is needed only for the estimate of the approximation accuracy). Then the qubit potential $U(\delta)$ [Eq. (2)] can be approximated by the cubic polynomial $\tilde{U}_c(\delta) = \sqrt{1 - \lambda^{-2}}E_J(\epsilon^2 y/2 - y^3/6)$, where a constant is neglected and

$$\epsilon = \sqrt{2(\phi_c - \phi)/\sqrt{\lambda^2 - 1}}. \quad (\text{A10})$$

The minimum and maximum of this potential are at $y_l = -\epsilon$ and $y_{\max} = \epsilon$, respectively, i.e., at

$$\delta_l = \delta_c - \epsilon, \quad \delta_{\max} = \delta_c + \epsilon. \quad (\text{A11})$$

Shifting the axis again as $x = y + \epsilon = \delta - \delta_c + \epsilon$ and again neglecting a constant, the qubit potential can be rewritten as

$$U_c(\delta) = \sqrt{1 - \lambda^{-2}}E_J(\epsilon x^2/2 - x^3/6). \quad (\text{A12})$$

In this approximation¹³ the left well parameters are

$$\omega_l = (1 - \lambda^{-2})^{1/4} \sqrt{\epsilon E_J/m}, \quad (\text{A13})$$

$$\Delta U_l = \frac{2}{3} \sqrt{1 - \lambda^{-2}} E_J \epsilon^3, \quad (\text{A14})$$

$$N_l = \frac{2}{3\hbar} (1 - \lambda^{-2})^{1/4} \sqrt{m E_J} \epsilon^{5/2}. \quad (\text{A15})$$

The validity condition for the cubic-potential description (A12) can be found by estimating the neglected y^4 term in Eq. (A9). Requiring that this term is much smaller than the y^3 term for $|y| \leq 2\epsilon$ (the region of interest for the potential), we find the condition $\epsilon \ll \sqrt{\lambda^2 - 1}$, which for $\lambda \geq 2$ simplifies to

$$\epsilon \ll \lambda, \quad (\text{A16})$$

and can also be translated into $\phi_c - \phi \ll \lambda^3$. This validity condition for the cubic-potential approximation is well satisfied for the qubit parameters considered in the present paper.

APPENDIX B: HAMILTONIAN FOR TWO CAPACITIVELY COUPLED QUBITS

In the absence of dissipation ($R_i = \infty$) the equations of motion (5) for two capacitively coupled qubits (Fig. 2) can be written in the form of Lagrange's equations,²⁰

$$\frac{d}{dt} \frac{\partial L}{\partial \dot{\delta}_i} - \frac{\partial L}{\partial \delta_i} = 0, \quad (\text{B1})$$

with the Lagrangian

$$L = K - U_1(\delta_1) - U_2(\delta_2). \quad (\text{B2})$$

Here the i th qubit potential energy is [cf. Eq. (2)]

$$U_i(\delta_i) = E_{ji} \left[\frac{(\delta_i - \phi_i)^2}{2\lambda_i} - \cos \delta_i \right], \quad (\text{B3})$$

where $E_{ji} = \Phi_0 I_{0i} / 2\pi$, $\lambda_i = 2\pi I_{0i} L_i / \Phi_0$, and the kinetic energy K is

$$K = \frac{m'_1 \dot{\delta}_1^2}{2} + \frac{m'_2 \dot{\delta}_2^2}{2} - m_x \dot{\delta}_1 \dot{\delta}_2, \quad (\text{B4})$$

where $m'_i = (\Phi_0 / 2\pi)^2 C'_i$ and $m_x = (\Phi_0 / 2\pi)^2 C_x$ are the normalized capacitances. Thus, the problem of two coupled qubits is equivalent to the motion of a fictitious particle in the two-dimensional space (δ_1, δ_2) . From Eqs. (B2) and (B4) one can obtain the generalized momenta $p_i = \partial L / \partial \dot{\delta}_i$ in the form

$$p_i = m'_i \dot{\delta}_i - m_x \dot{\delta}_j. \quad (\text{B5})$$

It is easy to see that p_i is the total (node) charge on the i th junction and the adjacent coupling capacitor multiplied by $\hbar/2e$.^{13,14} Dissipation can be accounted for by the addition²⁰ of the friction force F_i into r.h.s. of Eq. (B1). This yields Eq. (5) if

$$F_i = - \frac{\Phi_0^2}{4\pi^2 R_i} \dot{\delta}_i. \quad (\text{B6})$$

Equations (B5) can be inverted, yielding

$$\dot{\delta}_i = p_i / m''_i + p_j / m'_x, \quad (\text{B7})$$

where $m''_i = m_i + (m_j^{-1} + m_x^{-1})^{-1}$ and $m'_x = m_1 + m_2 + m_1 m_2 / m_x$. Inserting Eq. (B7) into (B4), one obtains the Hamiltonian²⁰ $H = K + U_1 + U_2$ in the form²⁴

$$H = \frac{p_1^2}{2m''_1} + \frac{p_2^2}{2m''_2} + \frac{p_1 p_2}{m'_x} + U_1(\delta_1) + U_2(\delta_2). \quad (\text{B8})$$

Notice that the Hamiltonian (B8) can also be derived in a direct way (without Lagrangian language) using the fact¹³ that the node charge (multiplied by $\hbar/2e$) p_i is the conjugated variable to the phase δ_i and expressing the combined electrostatic energy of capacitors C_1 , C_2 and C_x in the form of three first terms of Eq. (B8).

Instead of Lagrange's equations (B1), one can use Hamilton's equations²⁰ with respect to δ_i and p_i , viz., Eq. (B7) and $\dot{p}_i = -\partial H / \partial \delta_i$ or, in view of (B8),

$$\dot{p}_i = - \frac{\partial U_i}{\partial \delta_i}. \quad (\text{B9})$$

This equation can be extended to take dissipation into account by adding the friction force (B6):

$$\dot{p}_i = - \frac{\partial U_i}{\partial \delta_i} - \frac{\Phi_0^2}{4\pi^2 R_i} \dot{\delta}_i. \quad (\text{B10})$$

In the case of two identical qubits [Eq. (7)] Eqs. (B7) and (B8) become

$$H = \frac{p_1^2 + p_2^2 + 2\zeta p_1 p_2}{2m''} + U_1(\delta_1) + U_2(\delta_2), \quad (\text{B11})$$

$$\dot{\delta}_i = \frac{p_i + \zeta p_j}{m''}, \quad (\text{B12})$$

where $m'' = (1 + \zeta)m$ and $\zeta = C_x / (C + C_x)$.

APPENDIX C: FIRST-QUBIT DYNAMICS

Neglecting the back action from the second qubit, we can drop the second term in the numerator in Eq. (B12) for the first qubit ($i=1$),

$$\dot{\delta}_1 = p_1 / m'', \quad (\text{C1})$$

then Eq. (B10) gives the following approximate equation of motion for the first qubit:

$$\ddot{\delta}_1 + \frac{\dot{\delta}_1}{C''R} + \frac{2\pi I_0}{\Phi_0 C''} \sin \delta_1 + \frac{\delta_1 - \phi_1}{C''L} = 0, \quad (\text{C2})$$

where $C'' = (1 + \zeta)C$. This is obviously the usual equation for an isolated first qubit with capacitance C replaced by effective capacitance $C'' = C + C_x C / (C_x + C)$ which takes into account the series connection of the coupling capacitance and the second junction capacitance (this corresponds to the approximation of zero charge at the second qubit).

Note that even though the set of equations of motion (5) is equivalent to Eqs. (B7) and (B10), the above approximation makes them different. In particular, in the case of identical qubits the equation for the first qubit obtained from Eq. (5) by neglecting the r.h.s., differs from Eq. (C2) by the substitution $C'' \leftrightarrow C' = C + C_x$. However, for small dimensionless coupling ζ (which is the experimentally relevant case assumed here), the two equations differ by very small terms on

the order of ζ^2 . Physically, C' as the effective capacitance of the first qubit corresponds to the model in which the voltage across the second junction is neglected (in contrast to the neglected charge in the previous model).

Equation (C2) shows that the first qubit performs damped nonharmonic oscillations. Because of anharmonicity, the gradual decrease of the qubit energy $E_1 = m''\dot{\delta}_1^2/2 + U_1(\delta_1)$ due to dissipation leads to the gradual increase⁹ of the oscillation frequency f_d (driving the second qubit) which can be obtained as²⁰

$$f_d^{-1}(E_1) = \sqrt{2m''} \int_{a(E_1)}^{b(E_1)} \frac{d\delta_1}{\sqrt{E_1 - U_1(\delta_1)}}, \quad (\text{C3})$$

where a and b are the classical turning points.

APPENDIX D: DETAILS OF THE CLASSICAL APPROACH FOR THE SECOND QUBIT

In the approximation (C1), the second-qubit equation of motion follows from Eqs. (B12) and (B10) with $i=2$:

$$\ddot{\delta}_2 + \frac{\dot{\delta}_2}{(1+\zeta)T_1'} + \frac{2\pi I_0}{\Phi_0 C''} \sin \delta_2 + \frac{\delta_2 - \phi_2}{C''L} = \zeta \ddot{\delta}_1(t). \quad (\text{D1})$$

This equation [coinciding with Eq. (10)] has a simple physical meaning as an evolution of the second qubit with effective junction capacitance C'' , externally driven by the oscillating current $(\Phi_0/2\pi)\zeta C''\dot{\delta}_1$. However, considering oscillating voltage $(\Phi_0/2\pi)\dot{\delta}_1$ across the first junction coupled to the second qubit via capacitance C_x , one would expect the driving current to be $(\Phi_0/2\pi)C_x\dot{\delta}_1$ [as in Eq. (5)]. The relative difference between $\zeta C''$ and C_x is on the order of $\zeta^2 \ll 1$, which is the accuracy of treating two qubits separately.

Using the model of a harmonic oscillator for the second qubit and neglecting the damping ($T_1' = \infty$), we substitute Eq. (D1) by Eq. (11): $\ddot{x} + \omega_{l2}^2 x = \zeta \ddot{\delta}_1(t)$, where $x = \delta_2 - \delta_{l2}$, δ_{l2} is the left-well minimum position, and ω_{l2} is the unperturbed plasma frequency. Actually, the small-vibration frequency in Eq. (D1) is different from ω_{l2} due to the mass (capacitance) renormalization $m \rightarrow m''$, so that $\omega_{l2} \rightarrow \omega_{l2}/\sqrt{1+\zeta}$; however, for small coupling considered here ($\zeta \leq 1\%$) we neglect the difference. Correspondingly, the oscillator energy is $E_2 = m(\dot{x}^2 + \omega_{l2}^2 x^2)/2$ (here we also neglect the difference between m and m'') and can be found via Eq. (12).

The driving frequency $f_d = \omega_d/2\pi$ (frequency of $\dot{\delta}_1$ oscillations) increases in time and passes through exact resonance at moment t_c : $\omega_d(t_c) = \omega_{l2}$. Let us consider the vicinity of t_c and approximate $\dot{\delta}_1(t)$ as a harmonic signal $\dot{\delta}_1(t) = A(t)\exp(i\int^t \omega_d dt)$ with constant amplitude $A = A(t_c)$ and linearly varying frequency

$$\omega_d(t) = \omega_{l2} + \alpha(t - t_c), \quad (\text{D2})$$

with $\alpha = \dot{\omega}_d(t_c) > 0$ (we have neglected the complex-conjugated term and higher-order harmonics as being out of resonance). Thus the problem is reduced to passage of a

harmonic oscillator through resonance with a constant rate.^{22,28} Also assuming slow crossing, $\alpha \ll \omega_{l2}^2$, and shifting the lower endpoint of integration in Eq. (12) to $-\infty$ (which is a good approximation for $t_c \gg \sqrt{2/\alpha}$), we obtain

$$E_2(t) = E_0 F(\tilde{t}), \quad E_0 = \frac{\pi \zeta^2 m A^2}{\alpha}, \quad \tilde{t} = \frac{t - t_c}{\sqrt{2/\alpha}},$$

$$F(\tilde{t}) = \frac{1}{\pi} \left| \int_{-\infty}^{\tilde{t}} e^{i\eta^2} d\eta \right|^2 = \frac{1}{4} \left| 1 + \operatorname{erf}\left(\frac{\tilde{t}}{\sqrt{i}}\right) \right|^2. \quad (\text{D3})$$

Notice that the function $F(\tilde{t})$ with \tilde{t} proportional to a spatial coordinate describes the Fresnel diffraction²⁹ and has the following asymptotic dependence:

$$F(\tilde{t}) \approx 1 + \frac{\sin(\tilde{t}^2 - \pi/4)}{\sqrt{\pi\tilde{t}}} \quad \text{for } \tilde{t} \gg 1, \quad (\text{D4a})$$

$$F(\tilde{t}) \approx (4\pi\tilde{t}^2)^{-1} \quad \text{for } -\tilde{t} \gg 1. \quad (\text{D4b})$$

The oscillating term in Eq. (D4a) describes the beating between the oscillator and driving force frequencies, with the difference frequency increasing in time, $d(\tilde{t}^2)/dt = \alpha(t - t_c)$, and the amplitude of beating decreasing as $1/\tilde{t}$ [see the dashed line in Fig. 5(a)]. Notice that $F(0) = 1/4$, $F(\infty) = 1$, and the maximum value is $F(1.53) = 1.370$, so that E_0 is the long-time limit of the oscillator energy E_2 , while the maximum energy $E_{2,\max}$ is 1.37 times larger and therefore is given by Eq. (13).

For the parameters of Fig. 5 ($N_{l2} = 5$) we find from Fig. 4 that exact resonance between $f_d(t)$ and $\omega_{l2}/2\pi = 8.91$ GHz occurs at $t_c = 0.085 T_1$ (in particular, $t_c = 2.13$ ns for $T_1 = 25$ ns and $t_c = 43$ ns for $T_1 = 500$ ns) and $\alpha = 110 \text{ ns}^{-1}/T_1$. To compare Eq. (D3) with the numerical results, we also need the value of A . It can be estimated as $A = \omega_{l2}^2 \tilde{A}/2$, where \tilde{A} is the amplitude of $\dot{\delta}_1(t)$ oscillations at $t = t_c$ (the factor $1/2$ comes from our definition of A as half of the amplitude of $\dot{\delta}_1$ oscillations). Using the numerical result $\tilde{A} \approx 2.7$ corresponding to the resonance with the second qubit at $N_{l2} = 5$, we find $A = 4.3 \times 10^3 \text{ ns}^{-2}$ (this resonance happens at 121 GHz below the barrier top; \tilde{A} is defined as half of the full span of $\dot{\delta}_1$ oscillations—see Fig. 3). The dashed line in Fig. 5(a) shows the corresponding analytical result (D3). One can see that the analytics fits the oscillator energy at $t = t_c$ pretty well; however, the maximum energy $E_{2,\max}$ given by Eq. (13) is somewhat different from the numerical result: $E_{2,\max}/\hbar\omega_{l2} = 11.8$ versus 14.2 numerically. (The difference decreases with increase of T_1 : for $C_x = 5$ fF and $T_1 = 500$ ns the corresponding numbers are 235 and 242.) A noticeable discrepancy between the analytical and numerical results in Fig. 5(a) can be attributed mainly to the fact that A and α change with time, in contrast to the assumptions made in the derivation of Eq. (D3). It is interesting to notice that $A(t)$ initially increases because of the frequency f_d increase, while it starts to decrease at $t > 0.52 T_1$ (after reaching the maximum of $5.8 \times 10^3 \text{ ns}^{-2}$) because of \tilde{A} decrease. Actually, a good fit of the numerical results by the values of A obtained as A

$= (2\pi f_d)^2 \tilde{A}/2$ is quite surprising, because oscillations $\ddot{\delta}_1(t)$ are strongly non-harmonic (even having three maxima and three minima per period). We have also calculated A using some advanced analysis of $\ddot{\delta}_1(t)$ and found values very close to the simple estimate. (This other method is based on calculating Fourier transform of $\ddot{\delta}_1$ within a time interval around t_c , cutting off the spectrum above the minimum between the first and second Fourier peaks, calculating inverse Fourier transform, and finding the oscillation amplitude at $t = t_c$.)

An increase of N_{l2} leads to more efficient excitation of the second qubit. For example, for $N_{l2}=10$ and other parameters as in Fig. 5(a), the numerical maximum value of $E_{2,\max}/\hbar\omega_{l2}$ becomes 30.5 (more than twice larger compared to the case $N_{l2}=5$). This happens because of the decrease of $\alpha(t)$ and increase of $A(t)$ with time, and correspondingly with N_{l2} (see Fig. 4). [For $N_{l2}=10$ (so that $\omega_{l2}/2\pi=10.2$ GHz), we find $t_c=0.192 T_1$ (i.e., $t_c=4.8$ ns for $T_1=25$ ns and $t_c=96$ ns for $T_1=500$ ns), $\alpha=57$ ns $^{-1}/T_1$, and $A(t_c)=5.2 \times 10^3$ ns $^{-2}$.]

DETAILS OF THE QUANTUM APPROACH

In the quantum approach the second qubit can be described by the wave function $\Psi(\delta, t)$ (we omit the subscript 2 to shorten notations), which obeys the Schrödinger equation

$$i\hbar \frac{\partial \Psi}{\partial t} = H(t)\Psi. \quad (\text{E1})$$

Here the Hamiltonian

$$H(t) = \frac{\hat{p}^2 + 2\zeta p_1(t)\hat{p}}{2(1+\zeta)m} + U(\delta), \quad (\text{E2})$$

in which $\hat{p} = -i\hbar(\partial/\partial\delta)$, follows from Eq. (8) by considering p_2 as the operator \hat{p} , while $p_1(t)$ and $\delta_1(t)$ are considered as classical functions of time obtained from Eqs. (C2) and (C1); the first-qubit energy in this case does not contribute to the Hamiltonian (E2).

The term linear in \hat{p} in Eq. (E2) has the same form as for the interaction of a charged particle with a time-dependent electric field described by a vector potential.²⁹ Using the gauge transformation²³

$$\Psi(\delta, t) = \psi(\delta, t) e^{-i\zeta p_1(t)\delta/\hbar}, \quad (\text{E3})$$

we can replace the vector-potential by a scalar potential in the Hamiltonian. Then evolution of the wave function ψ is described by the Schrödinger equation (18) with the Hamiltonian $H_r(t)$ given by Eqs. (19) and (20), which consists³⁰ of the time-independent part $H_0 = \hat{p}^2/2m'' + U(\delta)$ and time-dependent part $V(t) = -\zeta m'' \ddot{\delta}_1(t)\delta$, where $m'' = (1+\zeta)m$. Notice that to obtain H_r in this form we have subtracted c -number term $\zeta^2 p_1^2(t)/(2m'')$ and used Eq. (C1).

The partial differential equation (18) for $\psi(\delta, t)$ can be reduced to an infinite set of ordinary differential equations²³ using the expansion (21) of the wave function ψ over the eigenfunctions $\psi_n(\delta)$ of H_0 : $\psi(\delta, t) = \sum_n a_n(t) \psi_n(\delta)$. Then the coefficients $a_n(t)$ evolve as

$$\dot{a}_n = -i(E_n/\hbar)a_n + \frac{i\zeta m'' \ddot{\delta}_1(t)}{\hbar} \sum_{n'} \delta_{nn'} a_{n'}, \quad (\text{E4})$$

where E_n is an eigenvalue of H_0 and $\delta_{nn'}$ is the ‘‘position’’ matrix element:

$$\delta_{nn'} = \int_{-\infty}^{\infty} \psi_n^*(\delta) \delta \psi_{n'}(\delta) d\delta \quad (\text{E5})$$

(notice that we will use a different notation for the Kronecker symbol).

We calculate the eigenstates and eigenvalues of H_0 numerically, using the Fourier grid Hamiltonian method³² (same as periodic pseudospectral method³³). After obtaining eigenfunctions, we calculate the matrix $\delta_{nn'}$ (E5) and solve numerically Eqs. (E4), restricting the space to a finite subset of the states. For a given N_{l2} , we take a reasonably small number n_r of consecutive states ($n = n_i, n_i+1, \dots, n_i+n_r$), which include all left-well states and provide a sufficiently good approximation to the exact solution (the choice of the subset of states is discussed below). The column vector $a = (a_{n_i}, \dots, a_{n_i+n_r})^T$ satisfies the equation [cf. Eq. (E4)]

$$i\hbar \dot{a} = \tilde{H}(t)a, \quad (\text{E6})$$

in which the matrix

$$\tilde{H}_{nn'}(t) = E_n \delta_{nn'}^K - \zeta m'' \ddot{\delta}_1(t) \delta_{nn'} \quad (n_i \leq n, n' \leq n_i + n_r), \quad (\text{E7})$$

is the Hamiltonian of the system in the restricted Hilbert space spanned by the subset of states (here $\delta_{nn'}^K$ is the Kronecker symbol).

Let us briefly discuss our choice of the restricted subset of n_r states used for the numerical solution of Eq. (E6). First, we consider the eigenvalues of $\tilde{H}_{nn'}$ (E7) as functions of $\ddot{\delta}_1$, and require that this dependence is sufficiently close to the dependence obtained using the full Hamiltonian [Eqs. (19) and (20)]. Besides comparing the energies, we also compare the matrix elements $\delta_{nn'}$ obtained using either the full or restricted space (now only for the maximum and minimum values of $\ddot{\delta}_1$), and require that the difference is below 1%. The calculations in Sec. V for the case $N_{l2}=5$ have been performed for the subset of $n_r=30$ states: $167 \leq n \leq 196$ (in this case there are 6 states localized in the left well: $n = 169, 171, \dots, 179$). For $N_{l2}=10$, we have used $n_r=45$

states: $141 \leq n \leq 185$. We have also performed calculations with enlarged subsets (up to $n_r=150$) and found that the switching probability varies irregularly with the number of

states in the subset; however, this variation is not significant, at least in the case of low switching probability $P_s \leq 0.3$, which is the range of our interest.

*Permanent address: Department of Chemical Physics, The Weizmann Institute of Science, Rehovot 76100, Israel.

- ¹J. M. Martinis, S. Nam, J. Aumentado, and C. Urbina, *Phys. Rev. Lett.* **89**, 117901 (2002); Y. Yu, S. Han, X. Chu, S.-I. Chu, and Z. Wang, *Science* **296**, 1869 (2002); A. J. Berkley, H. Xu, R. C. Ramos, M. A. Gubrud, F. W. Strauch, P. R. Johnson, J. R. Anderson, A. J. Dragt, C. J. Lobb, and F. C. Wellstood, *ibid.* **300**, 1548 (2003); J. Claudon, F. Balestro, F. W. J. Hekking, and O. Buisson, *Phys. Rev. Lett.* **93**, 187003 (2004).
- ²I. Chiorescu, Y. Nakamura, C. J. P. M. Harmans, and J. E. Mooij, *Science* **299**, 1869 (2003); J. R. Friedman, V. Patel, W. Chen, S. K. Tolpygo, and J. E. Lukens, *Nature (London)* **406**, 43 (2000); B. L. T. Plourde, T. L. Robertson, P. A. Reichardt, T. Hime, S. Linzen, C.-E. Wu, and J. Clarke, *Phys. Rev. B* **72**, 060506(R) (2005); T. Kutsuzawa, H. Tanaka, S. Saito, H. Nakano, K. Semba, and H. Takayanagi, *Appl. Phys. Lett.* **87**, 073501 (2005); E. Il'ichev, N. Oukhanski, A. Izmailkov, T. Wagner, M. Grajcar, H.-G. Meyer, A. Yu. Smirnov, A. Maassen van den Brink, M. H. S. Amin, and A. M. Zagorskin, *Phys. Rev. Lett.* **91**, 097906 (2003); W. D. Oliver, Y. Yu, J. C. Lee, K. L. Berggren, L. S. Levitov, and T. P. Orlando, *Science* **310**, 1653 (2005); A. O. Niskanen, K. Harrabi, F. Yoshihara, Y. Nakamura, and J. S. Tsai, cond-mat/0609627 (unpublished).
- ³Y. Nakamura, Yu. A. Pashkin, and J. S. Tsai, *Nature (London)* **398**, 786 (1999); D. Vion D, A. Aassime, A. Cottet, P. Joyez, H. Pothier, C. Urbina, D. Esteve, and M. H. Devoret, *Science* **296**, 886 (2002); T. Yamamoto, Yu. A. Pashkin, O. Astafiev, Y. Nakamura, and J. S. Tsai, *Nature (London)* **425**, 941 (2003); T. Duty, D. Gunnarsson, K. Bladh, and P. Delsing, *Phys. Rev. B* **69**, 140503(R) (2004); A. Guillaume, J. F. Schneiderman, P. Delsing, H. M. Bozler, and P. M. Echternach, *Phys. Rev. B* **69**, 132504 (2004); A. Wallraff, D. I. Schuster, A. Blais, L. Frunzio, J. Majer, M. H. Devoret, S. M. Girvin, and R. J. Schoelkopf, *Phys. Rev. Lett.* **95**, 060501 (2005).
- ⁴M. A. Nielsen and I. L. Chuang, *Quantum Computation and Quantum Information* (Cambridge University Press, Cambridge, 2000).
- ⁵R. W. Simmonds, K. M. Lang, D. A. Hite, S. Nam, D. P. Pappas, and J. M. Martinis, *Phys. Rev. Lett.* **93**, 077003 (2004).
- ⁶K. B. Cooper, M. Steffen, R. McDermott, R. W. Simmonds, S. Oh, D. A. Hite, D. P. Pappas, and J. M. Martinis, *Phys. Rev. Lett.* **93**, 180401 (2004).
- ⁷P. R. Johnson, W. T. Parsons, F. W. Strauch, J. R. Anderson, A. J. Dragt, C. J. Lobb, and F. C. Wellstood, *Phys. Rev. Lett.* **94**, 187004 (2005); **95**, 049901 (2005).
- ⁸J. Kempe and K. B. Whaley, *Phys. Rev. A* **65**, 052330 (2002).
- ⁹R. McDermott, R. W. Simmonds, M. Steffen, K. B. Cooper, K. Cicak, K. D. Osborn, S. Oh, D. P. Pappas, and J. M. Martinis, *Science* **307**, 1299 (2005).
- ¹⁰M. Steffen, M. Ansmann, R. C. Bialczak, N. Katz, E. Lucero, R. McDermott, M. Neeley, E. M. Weig, A. N. Cleland, and J. M. Martinis, *Science* **313**, 1423 (2006).
- ¹¹N. Katz *et al.*, *Science* **312**, 1498 (2006); M. Steffen *et al.*, *Phys. Rev. Lett.* **97**, 050502 (2006).
- ¹²A. Wallraff, D. I. Schuster, A. Blais, L. Frunzio, R.-S. Huang, J. Majer, S. Kumar, S. M. Girvin, and R. J. Schoelkopf, *Nature (London)* **431**, 162 (2004); I. Siddiqi, R. Vijay, F. Pierre, C. M. Wilson, L. Frunzio, M. Metcalfe, C. Rigetti, R. J. Schoelkopf, M. H. Devoret, D. Vion, and D. Esteve, *Phys. Rev. Lett.* **94**, 027005 (2005); I. Siddiqi, R. Vijay, M. Metcalfe, E. Boaknin, L. Frunzio, R. J. Schoelkopf, and M. H. Devoret, *Phys. Rev. B* **73**, 054510 (2006); T. Duty, G. Johansson, K. Bladh, D. Gunnarsson, C. Wilson, and P. Delsing, *Phys. Rev. Lett.* **95**, 206807 (2005); M. Sillanpaa, T. Lehtinen, A. Paila, Y. Makhlin, and P. Hakonen, *ibid.* **96**, 187002 (2006).
- ¹³K. K. Likharev, *Dynamics of Josephson Junctions and Circuits* (Gordon and Breach, New York, 1986); T. Van Duzer and C. W. Turner, *Principles of Superconductive Devices and Circuits* (Elsevier, New York, 1981); A. Barone and G. Paternó, *Physics and Applications of the Josephson Effect* (Wiley, New York, 1982).
- ¹⁴P. R. Johnson, F. W. Strauch, A. J. Dragt, R. C. Ramos, C. J. Lobb, J. R. Anderson, and F. C. Wellstood, *Phys. Rev. B* **67**, 020509(R) (2003).
- ¹⁵The chosen unrounded value for N_{I1} corresponds to a rounded value for another parameter $[(\phi_c - \phi_1)/\lambda]$ which we have used in the code.
- ¹⁶K. K. Likharev, *Physica B & C* **108**, 1079 (1981).
- ¹⁷Q. Zhang, A. G. Kofman, J. M. Martinis, and A. N. Korotkov, *Phys. Rev. B* **74**, 214518 (2006).
- ¹⁸N. Katz *et al.*, (unpublished).
- ¹⁹M. C. Gutzwiller, *Chaos in Classical and Quantum Mechanics* (Springer, New York, 1990).
- ²⁰L. D. Landau and E. M. Lifshitz, *Mechanics* (Pergamon, Oxford, 1976).
- ²¹Passage through resonance for a system with a quartic potential (a Duffing oscillator) was considered in Ref. 22 and in I. R. Collinge and J. R. Ockendon, *SIAM J. Appl. Math.* **37**, 350 (1979).
- ²²M. J. Ablowitz, B. A. Funk, and A. C. Newell, *Stud. Appl. Math.* **52**, 51 (1973).
- ²³L. D. Landau and E. M. Lifshitz, *Quantum Mechanics: Non-Relativistic Theory*(Pergamon, Oxford, 1977).
- ²⁴For coupled current-biased phase qubits, this Hamiltonian was obtained, e. g., in Refs. 25,14,26; similar Hamiltonian for coupled charge qubits was obtained, e. g., in Ref. 27.
- ²⁵A. Blais, A. Maassen van den Brink, and A. M. Zagorskin, *Phys. Rev. Lett.* **90**, 127901 (2003).
- ²⁶T. Wu, Z. Li, and J. Liu, *Jpn. J. Appl. Phys., Part 2* **45**, L180 (2006).
- ²⁷Yu. A. Pashkin, T. Yamamoto, O. Astafiev, Y. Nakamura, D. V. Averin, and J. S. Tsai, *Nature (London)* **421**, 823 (2003).
- ²⁸F. M. Lewis, *Trans. ASME* **54**, 253 (1932); J. Kevorkian, *SIAM J. Appl. Math.* **20**, 364 (1971); *SIAM J. Appl. Math.* **26**, 364 (1974).

²⁹L. D. Landau and E. M. Lifshitz, *The Classical Theory of Fields* (Pergamon, Oxford, 1975), sec. 60.

³⁰Alternatively, one can represent Eq. (E2) as $H(t)=H_0+V'(t)$, where $V'(t)$ is the term linear in \hat{p} . Note, however, that in this case (because of the “vector potential”), the generalized momentum \hat{p} differs from the kinetic momentum $m\hat{\delta}$ and hence H_0 [Eq. (19)] does not correspond to the classical energy [given by Eq. (16)]. Thus, the gauge without “vector potential” (without terms linear in \hat{p}) has the advantage that in contrast to other gauges, the coefficients of $\psi_n(\delta)$ in the expansion (21) of the

wave function have the physical meaning of the probability amplitudes for the energy eigenstates (Ref. 31).

³¹W. E. Lamb, Phys. Rev. **85**, 259 (1952); K.-H. Yang, Ann. Phys. **101**, 62 (1976); C. Leubner and P. Zoller, J. Phys. B **13**, 3613 (1980); W. E. Lamb, R. R. Schlicher, and M. O. Scully, Phys. Rev. A **36**, 2763 (1987).

³²C. C. Marston and G. G. Balint-Kurti, J. Chem. Phys. **91**, 3571 (1989).

³³B. Fornberg, *A Practical Guide to Pseudospectral Methods* (Cambridge University Press, Cambridge, 1996).